

# Single-exposure holographic 3D printing via inverse-designed phase masks

Dajun Lin<sup>1†</sup>, Xiaofeng Chen<sup>2†</sup>, Connor O. Dea<sup>2†</sup>, Ji-Won Kim<sup>2</sup>, Keldy S. Mason<sup>2</sup>, Kwong Sang Lee<sup>3</sup>, Apratim Majumder<sup>1</sup>, Chih-Hao Chang<sup>3</sup>, Michael Cullinan<sup>3\*</sup>, Zachariah A. Page<sup>2\*</sup>, Rajesh Menon<sup>1\*</sup>

<sup>1</sup>Department of Electrical & Computer Engineering, University of Utah, Salt Lake City & 84112, USA.

<sup>2</sup>Department of Chemistry, University of Texas at Austin, Austin & 78712, USA.

<sup>3</sup>Walker Department of Mechanical Engineering, University of Texas at Austin, Austin & 78712, USA.

\*Corresponding authors: rmenon@eng.utah.edu, zpage@cm.utexas.edu, michael.cullinan@austin.utexas.edu

†These authors contributed equally to this work.

**Additive manufacturing using light is commonly constrained by serial voxel-by-voxel or layer-by-layer processing, which fundamentally limits fabrication speed and scalability. Here, we introduce a single-exposure holographic three-dimensional (3D) printing approach that synthesizes an entire volumetric dose distribution optically in one step. The method combines inverse-designed microstructured phase masks with photopolymer resins engineered for controlled optical absorption. By precisely tailoring the phase-mask topography, we generate arbitrary 3D light-intensity distributions within the resin, including intentionally encoded dark regions that define hollow internal features. Simultaneously, the resin formulation is designed to balance optical penetration with sufficient local energy deposition to achieve high-fidelity polymerization throughout the volume. Using this approach, millimeter-scale architectures comprising more than  $10^6$**

**addressable voxels are fabricated in a single 7.5 s exposure, corresponding to a volumetric throughput of  $\sim 1 \text{ mm}^3/\text{s}$  ( $> 10^5$  voxels/s). The demonstrated performance is presently limited by resin kinetics and illumination geometry rather than by the phase-mask framework itself. Because the volumetric information capacity scales with the space-bandwidth product of the phase mask, this approach provides a clear pathway toward substantially higher throughput, enabling scalable fabrication of micro-optical components, biomedical scaffolds, and other precision-engineered mesoscale systems.**

Additive manufacturing (AM), also known as three-dimensional (3D) printing, has transformed the fabrication of complex volumetric structures, enabling unprecedented design freedom across disciplines ranging from electronics and photonics to biomedicine and microelectromechanical systems (MEMS) (1). Among AM approaches, stereolithography (SLA) achieves 3D structuring by spatially confining photopolymerization through linear absorption and optical attenuation, typically via layer-by-layer exposure. SLA benefits from simple optical architectures and moderate illumination intensities ( $\sim 1\text{--}10^3 \text{ W/cm}^2$ ), but strong absorption and undesired out-of-plane curing fundamentally restricts it to ultrathin structures (2, 3).

Nonlinear optical approaches such as 2-photon polymerization overcome these limitations by providing true volumetric confinement of polymerization. However, they require ultrahigh peak intensities ( $10^9\text{--}10^{12} \text{ W/cm}^2$ ) and rely on intrinsically serial fabrication, resulting in slow volumetric build rates ( $\sim 0.01 \text{ mm}^3/\text{h}$ ) that severely limit scalability (4–7). Recent advances in molecular engineering have partially relaxed these constraints by enabling two-step absorption mechanisms that decouple optical excitation from polymerization. Implemented using either single-color (8) or two-color excitation schemes (9), these approaches reduce the required light intensities to  $\sim 10^6 \text{ W/cm}^2$  while improving spatial control over reaction initiation. Nevertheless, all methods rely on sequential exposures—through focal scanning or stacked projections—imposing fundamental limits on printing speed, scalability, and system complexity.

To address these throughput limitations, significant effort has focused on accelerating SLA-based processes. Digital light processing (DLP) projects entire two-dimensional patterns simultaneously at low illumination intensities ( $\sim 10^{-3}\text{--}10^{-1} \text{ W/cm}^2$ ), enabling high-throughput printing rates of  $\sim 3\text{--}50 \text{ mm}^3/\text{s}$  via layer-wise or continuous exposure schemes (10–12). Subsequent

advances have extended DLP to roll-to-roll manufacturing platforms (13) and to microscale resolutions (14). Alternatively, parallelized focused-laser exposure schemes have been developed to preserve submicrometer resolution while increasing throughput, though they continue to require costly ultrahigh-intensity laser systems (15). Despite these advances, all such approaches remain fundamentally constrained by repeated light exposures, precluding full volumetric parallelization.

An alternative paradigm is volumetric printing (Fig. 1A), including computed axial lithography (CAL) and xolography, which reconstruct entire 3D objects by accumulating dose through multiple projections, moving light sheets, or dynamically modulated fields (16–19). By integrating sequential exposures from different projection angles, CAL enables rapid fabrication of centimeter-scale objects in under a minute, achieving volumetric build rates comparable to state-of-the-art DLP systems ( $\sim 3$ – $50$  mm $^3$ /s). Further acceleration has been demonstrated using multi-axis illumination, enabling full-object formation in less than 10 s (20). However, these methods require complex optical assemblies, precise calibration, and tight synchronization, presenting challenges for robustness and widespread deployment.

Here we introduce a volumetric AM framework that enables mm-scale 3D microstructures to be fabricated in a single holographic exposure (Fig. 1B). In contrast to layer-by-layer or tomographic approaches, our method projects the entire 3D intensity distribution—the hologram—into the photoresin in one step. This is accomplished using a single inverse-designed phase mask that encodes the full 3D geometry, allowing complex solid and void architectures to be polymerized simultaneously. Unlike CAL or xolography, in which structure formation emerges from thresholded dose accumulation, our approach explicitly encodes both material and void regions directly into the optical field.

As a demonstration, we fabricate hollow 3D structures with a volume of 1.8 $^3$  mm $^3$  using a single 7.5-s exposure, and a voxel size of 24 $^3$   $\mu$ m $^3$ . This corresponds to approximately  $0.42 \times 10^6$  addressable voxels and a fabrication rate of  $0.55 \times 10^5$  voxels/s. The corresponding phase mask has an area of 2.4 $^2$  mm $^2$  and a pixel pitch of 1.5  $\mu$ m, yielding a space-bandwidth product (SBP) of  $2.56 \times 10^6$ , already exceeding that of typical spatial-light modulators (SLMs). The SBP defines the information capacity of the phase mask (21) and therefore, sets an upper bound on the number of independently addressable voxels. Notably, this proof-of-concept is limited by the  $\sim$ 3-mm diameter of the illumination beam rather than by any fundamental constraint. With higher laser power and

improved beam delivery, the approach readily scales to phase masks with areas of  $25^2 \text{ mm}^2$  and  $1-\mu\text{m}^2$  pixels, corresponding to an SBP of  $6.25 \times 10^8$ , far beyond what is achievable with SLM-based systems. While the passive nature of the phase mask is well suited for volume manufacturing of fixed designs, the same inverse-design framework can be extended to dynamic operation using SLMs, subject to their intrinsic constraints. Phase-mask fabrication further relies on mature manufacturing processes already deployed at scale in consumer electronics and security holography, enabling cost-effective, large-volume production (22). Because the phase mask is placed directly adjacent to the resin without intervening relay optics, the zero-order contribution is naturally incorporated and optimized during inverse design rather than filtered downstream, further simplifying the optical system.

The resolution of our approach is set by both the numerical aperture (NA) of the phase mask and the sampling period used during inverse design. For  $\lambda = 405 \text{ nm}$  and a pixel size  $w = 1.5 \mu\text{m}$ , the phase-mask NA is  $\lambda/(2w) = 0.135$ . This yields a diffraction-limited transverse resolution of  $\sim 3 \mu\text{m}$ , which is superseded here by the chosen sampling period of  $24 \mu\text{m}$ . The axial resolution is determined by the depth of focus  $\sim \lambda/\text{NA}^2 \approx 22 \mu\text{m}$ .

## Inverse design

Inverse design refers to the process of specifying an optical element by first defining a desired target function—such as a 3D light intensity distribution—and then computationally optimizing the design to achieve it (22–24). Prior studies have demonstrated that carefully engineered microstructures on a phase mask can be used to shape complex 3D light fields (25–30). This approach enables the generation of arbitrary volumetric intensity patterns, constrained only by diffraction and the SBP of the phase mask. Notably, since our phase masks are fabricated using lithography, they can achieve substantially higher SBP than traditional spatial-light modulators (as noted earlier), enabling finer spatial control and larger pattern volumes. We also note that recent holographic approaches either realize 3D structures through mechanical translation of a 2D field, as in acoustic holography, (31) or synthesize volumetric dose distributions sequentially using dynamically modulated optical elements such as DMDs or SLMs. (18) In contrast, our approach employs a single static, inverse-designed optical phase mask to directly generate the complete 3D light-dose distribution in a single exposure,

with void regions explicitly encoded in the optical field.

To generate the target 3D intensity distribution, we begin by preprocessing the input geometry, as illustrated in Fig. 2. A computer-aided design (CAD) model, typically spanning  $\approx 2^3 \text{ mm}^3$ , is imported and axially sliced into a user-defined number of layers to ensure structural continuity. Each slice is then discretized using a Gaussian-dot-shaped sampling grid, with full width at half maximum (FWHM)  $4 \mu\text{m}$  and inter-dot spacing of  $24 \mu\text{m}$  (Fig. 2A). This sampling strategy enhances axial resolution and enables fine control over energy deposition. By optimizing the peak intensity and spatial arrangement of the dots, we further improve the fidelity of the reconstructed pattern. Detailed analysis including comparisons to a continuous pattern and of the influence of dot spacing, shape, and size are provided in the Supplementary Notes S1-S3. To highlight the versatility of the inverse design process in shaping complex 3D light fields, we include simulated reconstructions of standard benchmark geometries in Supplementary Notes S7-S8. Throughout this work, the effective voxel size is defined by the hologram sampling period,  $24 \mu\text{m}$  in all three dimensions. This value is slightly larger than the depth-of-focus of the phase mask, ensuring that adjacent voxels remain optically resolvable while maintaining robust curing contrast.

The inverse design of the phase mask is implemented using the TensorFlow framework (v2.10, Google Inc.). In the example shown, the phase mask spans  $2.4 \text{ mm} \times 2.4 \text{ mm}$ , consisting of  $1600 \times 1600$  pixels with  $1.5 \mu\text{m}$ -wide square pixels, and a maximum height of  $587 \text{ nm}$ , optimized for a working wavelength of  $405 \text{ nm}$ . The phase modulation is defined as:

$$t(x, y) = \exp\left(\frac{j2\pi h(x, y)\Delta n}{\lambda}\right), \quad (1)$$

where  $h(x, y)$  is the height profile to be optimized,  $\lambda$  is the wavelength, and  $\Delta n$  is the refractive index contrast between the photoresist and air.

Light propagation from the phase mask to the resin is modeled using the angular-spectrum method across a user-defined gap (in the example shown, gap =  $5 \text{ mm}$ ), yielding the intensity distributions  $I(Z_i)$  at a set of axial planes. The objective of the inverse design is to minimize the discrepancy between the simulated volumetric intensity and the target 3D distribution. This is achieved by minimizing a weighted sum of mean squared errors (MSEs) across all slices:

$$\text{Loss} = \sum_{i=1}^n w(Z_i) \cdot (I(Z_i) - \alpha T(Z_i))^2, \quad (2)$$

where  $T(Z_i)$  is the target intensity at depth  $Z_i$ ,  $\alpha$  is a normalization factor, and  $w(Z_i)$  are slice-specific weights. The procedure for parameter optimization is described in Supplementary Note S11. The forward light propagation model is fully differentiable, and the loss gradient is calculated for back-propagation during optimization. The optimization is terminated when the loss function value decreases by less than 0.1%. Attenuation within the resin is compensated using an exponential intensity correction derived from the Beer–Lambert law (see Supplementary Note S9).

## Experiments

The phase mask was fabricated on a 2-inch glass wafer using grayscale lithography, following procedures described previously (22, 32). Fabrication fidelity was verified by measuring the surface topography using scanning confocal microscopy (Olympus LEXT OLS5000; Fig. 2E). The mask was illuminated with a collimated 405 nm laser (100 mW, Edmund Optics, #19-462) using the optical configuration shown in Fig. 3A. The resulting 3D light-intensity distribution was experimentally characterized by axially scanning an image sensor (Supplementary Information Notes S5 and S12), with a representative reconstructed volume shown in Fig. 2C. The measured hologram exhibits needle-like intensity columns aligned with the optical axis, a direct consequence of the Gaussian dot-sampling strategy employed in the inverse design. Magnified views of the pillar and central hollow regions (Fig. 2D) confirm strong spatial confinement of the optical field.

Although residual intensity is present within nominally dark (hollow) regions, its magnitude is substantially lower than that within the target volume. To suppress spurious polymerization inside the hollow core, the optical intensity in these regions must remain below the resin curing threshold. We quantify the layer-wise image contrast as

$$K = \frac{I_{\text{inside}} - I_{\text{outside}}}{I_{\text{inside}} + I_{\text{outside}}}, \quad (3)$$

where  $I_{\text{inside}}$  and  $I_{\text{outside}}$  denote the average intensity inside and outside the target region, respectively. From the measured volumetric intensity distributions (Figs. 2C and D), we extracted contrasts of 21%, 30%, and 20% at representative axial planes corresponding to  $z = 5$  mm (ring),  $z = 5.5$  mm (pillars), and  $z = 6$  mm (ring), respectively. These contrast levels are sufficient to resolve the hollow-cylinder geometry during photopolymerization. Each pillar arises from a superposition of discrete focal spots that locally overcome  $\text{O}_2$  inhibition, while background illumination within both

the central void and surrounding regions remains below threshold, thereby minimizing unintended curing and preserving spatial resolution.

As illustrated in Fig. 3A, the collimated 405 nm beam was expanded and aligned to uniformly illuminate the phase mask. A square aperture placed upstream of the mask suppressed stray light and defined clean beam boundaries, while a precision shutter controlled the exposure duration. An optical relay system projected the synthesized intensity distribution onto a CMOS sensor, enabling system alignment, pattern verification, and real-time monitoring of resin polymerization. Conjugate planes (purple dashed lines) established 1:1 magnification between the projected light field and the sensor, allowing accurate axial mapping and registration of the resin volume with the 3D intensity distribution. The phase mask was mounted at the base of the setup, with the resin contained in a standard petri dish positioned ~5 mm above the mask plane (alignment protocol is in Supplementary Notes S13-S14). The optically flat, thin dish bottom minimized distortion and preserved uniform axial resolution.

Optimization of the phase-mask design and exposure conditions was guided by two-dimensional projection experiments. Gaussian dot-array patterns were projected onto a 12- $\mu\text{m}$ -thick resin film, and the resulting refractive-index changes during curing were visualized in real time (Supplementary Note S17, S18). Dot arrays with sampling gaps of 0  $\mu\text{m}$  (continuous), 12  $\mu\text{m}$ , 18  $\mu\text{m}$ , and 24  $\mu\text{m}$  were evaluated using a 405 nm LED-DMD optical microscope under mean intensities of 10–40 mW/cm<sup>2</sup> and peak intensities of 120–700 mW/cm<sup>2</sup> (Supplementary Note S17). Exposure durations ranging from 0.8 to 40 s were selected based on real-time FTIR measurements of polymerization kinetics for the optimized resin formulation (Supplementary Note S10, S19). The resin consisted of bisacylphosphine oxide (BAPO; 0.46 mM, 0.017 wt%) dissolved in a di-pentaerythritol pentaacrylate/2-phenoxyethyl acrylate mixture (9:1 w:w), chosen for its high reactivity, high viscosity and favorable transmittance at 405 nm. These imaging-guided studies revealed that higher intensities and larger dot spacings, up to 24  $\mu\text{m}$ , improved curing fidelity and contrast (Supplementary Note S18). Accordingly, phase masks with a 24  $\mu\text{m}$  sampling period and a mean hologram intensity of ~50 mW/cm<sup>2</sup> were used in subsequent 3D printing experiments. This sampling period closely matches the diffraction-limited depth-of-focus of the phase mask, as discussed earlier.

To translate the optimized two-dimensional conditions to volumetric printing, it was necessary to control the evolution of the light field through the full resin depth. Optical attenuation was

compensated by tuning the BAPO concentration (extinction coefficient  $\epsilon_{405\text{ nm}} = 546 \text{ M}^{-1}\text{cm}^{-1}$ ) such that the peak intensity delivered by the grayscale phase mask at the final design depth ( $z = 2 \text{ mm}$ ) matched that at the entrance plane ( $z = 0 \text{ mm}$ ), as detailed in Supplementary Note S9. Using the experimentally measured mask grayscale ratio of  $\sim 1.1:1$ , a resin containing 0.46 mM BAPO (0.017 wt%) was formulated and used for all holographic printing experiments shown in Fig. 3.

Representative printed geometries, including a hollow cylinder and a cube, are shown in Figs. 3B–E. The structure in Fig. 3D was fabricated using a single 7.5 s exposure, whereas those in Figs. 3B, C, and E required 15 s due to reduced illumination intensity under a slightly modified optical configuration. All samples were developed by immersion in isopropyl alcohol at 45°C to remove uncured resin and subsequently post-cured for 30 s using a 405 nm LED. The devices shown in Figs. 3C and E were fabricated using a resin thickness exceeding the nominal design depth, yielding structures with volumes of  $\sim 1.8 \times 1.8 \times 3.6 \text{ mm}^3$ . Under these conditions, axial repetition of the holographically synthesized intensity pattern gives rise to additional ring features. These artifacts are not intrinsic to the target geometry and can be suppressed by restricting the resin thickness to the designed axial extent. Nevertheless, these results demonstrate potential for creating thicker devices.

Real-time monitoring of the polymerization process was performed using 850 nm illumination and a long-pass–filtered imaging system (Fig. 3A). As polymerization proceeds, cured regions scatter more 850 nm light than uncured resin, providing a direct optical signature of exposure progression. Time-lapse images of a hollow-cylinder print (Fig. 3F and Supplementary Video 1) illustrate this process, enabling adaptive control of the exposure time based on the observed contrast evolution.

## Discussion

Single-exposure 3D printing has been largely confined to structures that coincide with optical eigenmodes in homogeneous media, such as orbital angular momentum beams (33, 34), Bessel beams (35), and self-focused filaments (36), which inherently limits geometry to specific symmetries. By contrast, our inverse-designed holographic strategy enables single-shot fabrication of

arbitrary volumetric architectures without symmetry constraints. Simulations and imaging experiments of the “Benchy” geometry (Supplementary Note S8) further demonstrate this generality.

Volumetric light fields can be realized using dynamic SLMs or static phase masks (37–39). SLMs offer reconfigurability but are fundamentally constrained by limited space–bandwidth product (SBP  $\sim 10^6$ ), coarse pixel pitch ( $> 10 \mu\text{m}$ ), and low damage thresholds. These constraints limit the number of addressable voxels, transverse/axial resolution, and achievable print rates. Inverse-designed phase masks, in contrast, can be fabricated with sub- $\mu\text{m}$  pixel pitches (22, 40) and with large diameters (41), yielding SBPs  $> 10^8$  and high NA. Furthermore, phase masks can handle high-peak-power, ultrafast illumination (42), a regime essential for high-throughput printing (43). Direct placement adjacent to the resin further simplifies the optical setup.

A central element of our inverse design is discretizing target volumes into grids of Gaussian-like focal points that converge and diverge along the propagation axis. This sampling produces high peak-intensity tightly focused spots within a low-intensity background, generating radicals selectively while allowing O<sub>2</sub> inhibition to suppress off-target curing, thereby enhancing both axial and lateral resolution relative to continuous intensity distributions (Supplementary Notes S1–S4). Discrete sampling introduces additional design considerations: closely spaced focal points can partially reconstruct nondiffracting profiles reminiscent of Bessel beams, causing unintended morphologies and accelerated curing of vertical relative to horizontal features, possibly amplified by weak waveguiding in curing resin. Introducing angular diversity mitigates these effects, as shown in the tilted “U” geometry (Supplementary Fig. S11).

Optical attenuation within the resin also influences performance. The BAPO concentration (0.46 mol/m<sup>3</sup>) used here balances absorption with penetration depth. Increasing initiator loading can accelerate kinetics, sharpen thresholding, and improve mechanical robustness by increasing crosslink density, but at the cost of stronger attenuation and reduced contrast, necessitating a balance between axial uniformity, resolution, and mechanical integrity.

Lastly, although speckle is a common concern in holography, we observe no reduction in print fidelity, and established phase-randomization techniques can suppress speckle when necessary (44).

## Conclusion

In summary, we have demonstrated a single-exposure holographic additive manufacturing platform that circumvents the intrinsic speed limitations of serial and layer-by-layer 3D printing. By integrating inverse-designed phase masks with resin formulations engineered for controlled axial dose delivery, we achieved volumetric fabrication of mm-scale architectures with  $\sim 24 \mu\text{m}$  voxel resolution in a single 7.5 s exposure. This corresponds to a demonstrated throughput of  $\sim 1 \text{ mm}^3/\text{s}$  ( $10^5$  voxels/s). The approach is inherently scalable. Increasing the lateral extent of the phase mask while maintaining  $\sim 1 \mu\text{m}$  pixel pitch can substantially increase the SBP to  $> 10^8$ , thereby expanding the number of addressable voxels in a single exposure. Further gains in throughput to  $> 10^8$  voxels/s are expected from improved beam delivery and faster photochemical systems, (45) without altering the underlying optical framework. Because the achievable resolution is set by the NA of the phase mask, large-scale inverse design also enables increasingly complex geometries with diffraction-limited fidelity. Together, these results establish a general pathway toward high-speed, fully parallelized volumetric manufacturing, with potential applications spanning micro-optical components, biomedical scaffolds, and other precision-engineered mesoscale systems.

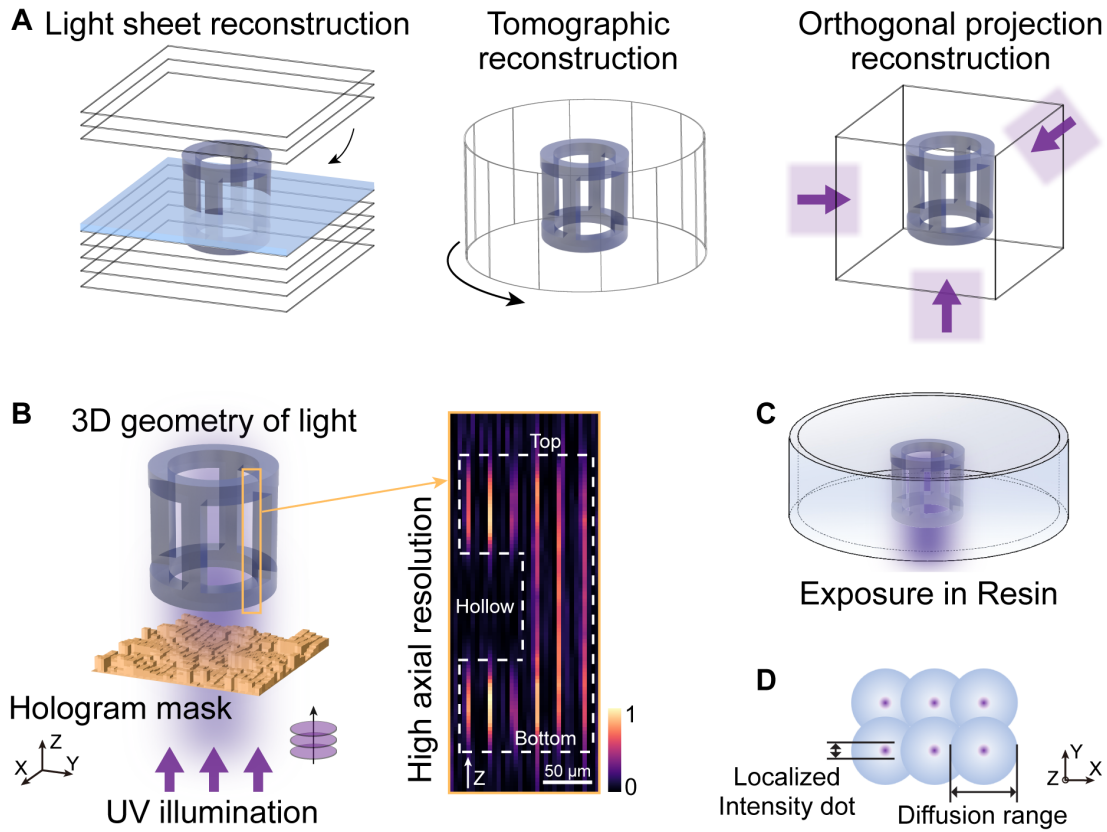


**Figure 1: Single-exposure holographic additive manufacturing.** (A) State-of-the-art volumetric fabrication rely on multiple exposures via scanning light-sheets, via tomographic (angle-resolved) projections into a rotating vat containing resin, or via orthogonal multi-angle beam projections. (B) In contrast, our approach generates arbitrary 3D holographic intensity distributions using a static phase mask. The mask encodes volumetric information via a spatial sampling grid for high axial resolution. In our demonstration, the mask, fabricated via grayscale lithography, measures  $2.4 \times 2.4 \text{ mm}^2$  with  $1.5 \mu\text{m}$  minimum features. Right panel shows a small portion of the simulated 3D holographic light distribution of the hollow cylinder illustrating high axial resolution (see details in Fig. 2). (C) The computed 3D intensity distribution is projected into a UV-curable resin, enabling simultaneous volumetric polymerization in a single exposure. (D) Mask and resin parameters are co-optimized to ensure localized light distributions (Gaussian “dots”) merge into a continuous 3D structure upon exposure.

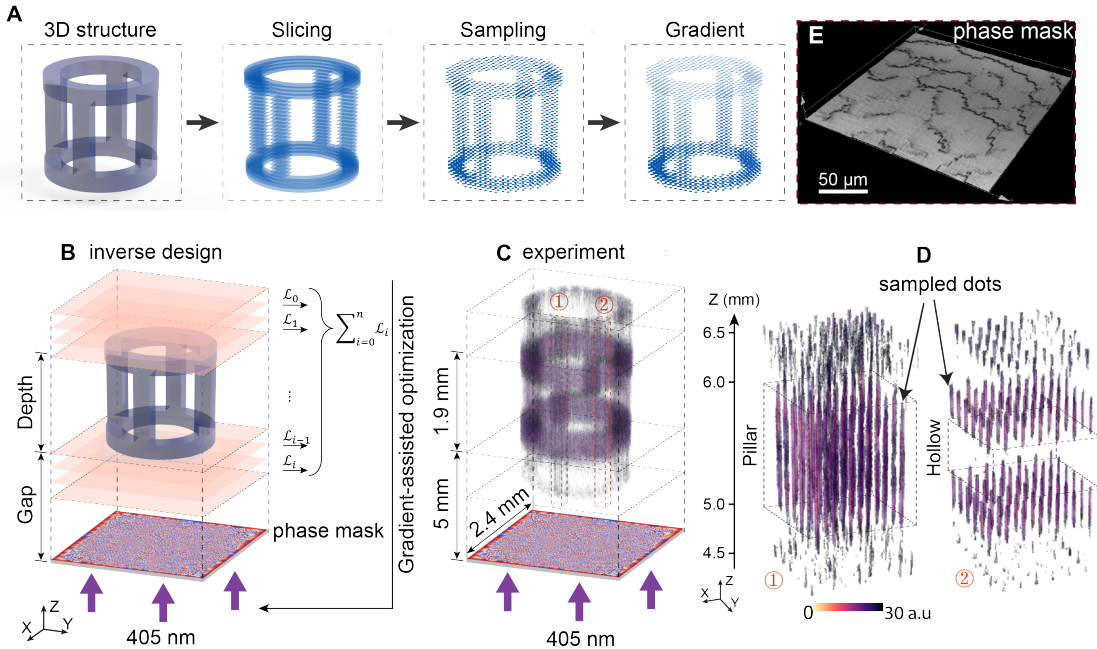


**Figure 2: Inverse design of the phase mask for single-shot 3D fabrication.** (A) Workflow for generating 3D target intensity distributions from computer-aided design (CAD) models. The continuous volumetric geometry is first discretized into axial slices along the light propagation direction. Each slice is then sampled using Gaussian focal spots, and a depth-dependent intensity gradient is applied to compensate for optical attenuation within the photoresin. (B) Inverse-design framework for phase-mask optimization. A depth-averaged loss function is minimized by iteratively updating the phase mask using back-propagated loss gradients, in direct analogy to gradient-based optimization in deep learning. (C) Measured 3D holographic intensity distribution, showing solid pillars and a hollow cylindrical core. (D) Magnified intensity maps from pillar and non-pillar regions, resolving individual sampled dots and confirming the absence of light in the hollow wall. (E) Optical micrograph of a representative region of an exemplary phase mask.

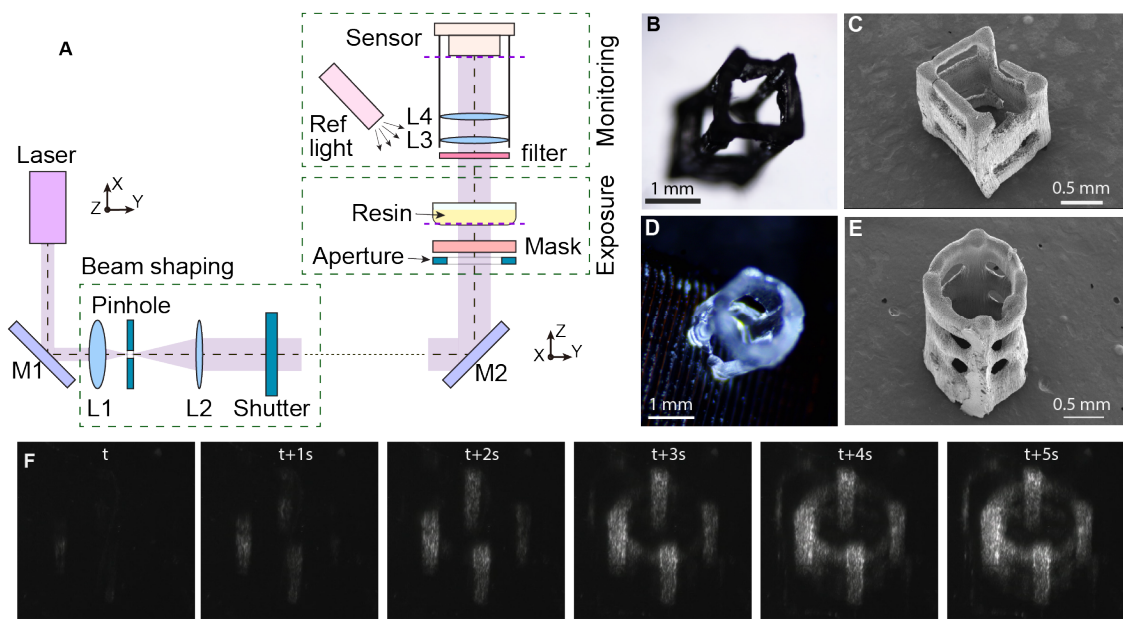


**Figure 3: Single-exposure holographic 3D printing.** A, Schematic of the experimental setup, where a shutter controls exposure duration. B–E, Optical and scanning electron micrographs of representative structures, a hollow cylinder and a cube, fabricated in a single exposure. Prints in B, C, and E used 15 s exposures, while D was produced in 7.5 s. The multiple windows visible in C and E arise when the resin thickness exceeds the designed volume. F, Time-lapse images of the hollow cylinder, recorded at 1 s intervals, reveal real-time progression of polymerization. Illumination was provided at 850 nm, with a long-pass filter before the camera to enhance contrast.

## References and Notes

1. A. Jadhav, V. S. Jadhav, A review on 3D printing: An additive manufacturing technology. *Materials Today: Proceedings* **62**, 2094–2099 (2022).
2. S. Maruo, K. Ikuta, Three-dimensional microfabrication by use of single-photon-absorbed polymerization. *Appl. Phys. Lett.* **76** (19), 2656 (2000).
3. M. T. Do, *et al.*, Submicrometer 3D structures fabrication enabled by one-photon absorption direct laser writing. *Optics express* **21** (18), 20964–20973 (2013).
4. X. Zhou, Y. Hou, J. Lin, A review on the processing accuracy of two-photon polymerization. *Aip Advances* **5** (3) (2015).
5. E. Skliutas, *et al.*, Polymerization mechanisms initiated by spatio-temporally confined light. *Nanophotonics* **10** (4), 1211–1242 (2021).
6. D. M. Wirth, C. C. Li, J. K. Pokorski, H. K. Taylor, M. Shusteff, Fundamental scaling relationships in additive manufacturing and their implications for future manufacturing and bio-manufacturing systems. *Additive Manufacturing* **84**, 104081 (2024).
7. L. Yang, *et al.*, Projection two-photon polymerization using a spatial light modulator. *Optics Communications* **331**, 82–86 (2014).
8. V. Hahn, *et al.*, Two-step absorption instead of two-photon absorption in 3D nanoprinting. *Nature Photonics* **15** (12), 932–938 (2021).
9. V. Hahn, *et al.*, Light-sheet 3D microprinting via two-colour two-step absorption. *Nature Photonics* **16** (11), 784–791 (2022).
10. Z. Zhao, X. Tian, X. Song, Engineering materials with light: recent progress in digital light processing based 3D printing. *Journal of Materials Chemistry C* **8** (40), 13896–13917 (2020).
11. J. R. Tumbleston, *et al.*, Continuous liquid interface production of 3D objects. *Science* **347** (6228), 1349–1352 (2015).

12. R. Janusziewicz, J. R. Tumbleston, A. L. Quintanilla, S. J. Mecham, J. M. DeSimone, Layerless fabrication with continuous liquid interface production. *Proceedings of the National Academy of Sciences* **113** (42), 11703–11708 (2016).
13. J. M. Kronenfeld, L. Rother, M. A. Saccone, M. T. Dulay, J. M. DeSimone, Roll-to-roll, high-resolution 3D printing of shape-specific particles. *Nature* **627** (8003), 306–312 (2024).
14. K. Hsiao, *et al.*, Single-digit-micrometer-resolution continuous liquid interface production. *Science advances* **8** (46), eabq2846 (2022).
15. W. Ouyang, *et al.*, Ultrafast 3D nanofabrication via digital holography. *Nature Communications* **14** (1), 1716 (2023).
16. M. Regehly, *et al.*, Xolography for linear volumetric 3D printing. *Nature* **588** (7839), 620–624 (2020).
17. D. Loterie, P. Delrot, C. Moser, High-resolution tomographic volumetric additive manufacturing. *Nature communications* **11** (1), 852 (2020).
18. M. I. Álvarez-Castaño, *et al.*, Holographic tomographic volumetric additive manufacturing. *Nature Communications* **16** (1), 1551 (2025).
19. I. Bhattacharya, J. Toombs, H. Taylor, High fidelity volumetric additive manufacturing. *Additive Manufacturing* **47**, 102299 (2021).
20. M. Shusteff, *et al.*, One-step volumetric additive manufacturing of complex polymer structures. *Science advances* **3** (12), eaao5496 (2017).
21. M. A. Neifeld, Information, resolution, and space–bandwidth product. *Optics letters* **23** (18), 1477–1479 (1998).
22. R. Menon, N. Brimhall, Perspectives on imaging with diffractive flat optics. *ACS Photonics* **10** (4), 1046–1052 (2023).
23. R. Menon, P. Wang, Nanophotonic scattering structure (2015), uS Patent 8,953,239.
24. S. Molesky, *et al.*, Inverse design in nanophotonics. *Nature Photonics* **12** (11), 659–670 (2018).

25. P. Wang, R. Menon, Optical microlithography on oblique and multiplane surfaces using diffractive phase masks. *Journal of Micro/Nanolithography, MEMS, and MOEMS* **14** (2), 023507–023507 (2015).
26. R. Menon, P. Wang, Methods and systems for generating a three-dimensional holographic mask having topographical pattern with more than two discrete levels (2020), uS Patent 10,571,861.
27. N. Mohammad, M. Meem, X. Wan, R. Menon, Full-color, large area, transmissive holograms enabled by multi-level diffractive optics. *Scientific reports* **7** (1), 5789 (2017).
28. S. Banerji, M. Meem, A. Majumder, B. Sensale-Rodriguez, R. Menon, Extreme-depth-of-focus imaging with a flat lens. *Optica* **7** (3), 214–217 (2020).
29. K. Sun, *et al.*, Three-dimensional direct lithography of stable perovskite nanocrystals in glass. *Science* **375** (6578), 307–310 (2022).
30. D. Lin, A. Majumder, P. Lu, R. Menon, Diffraction-free orbital angular momentum holography. *Optics Express* **33** (3), 5791–5799 (2025).
31. M. Derayatifar, M. Habibi, R. Bhat, M. Packirisamy, Holographic direct sound printing. *Nature Communications* **15** (1), 6691 (2024).
32. D. Lin, *et al.*, Inverse-designed multi-level diffractive doublet for wide field-of-view imaging. *ACS Photonics* **10** (8), 2661–2669 (2023).
33. L. Yang, *et al.*, Direct laser writing of complex microtubes using femtosecond vortex beams. *Applied Physics Letters* **110** (22) (2017).
34. H. Cheng, *et al.*, High-throughput microfabrication of axially tunable helices. *Photonics Research* **10** (2), 303–315 (2022).
35. H. Cheng, C. Xia, M. Zhang, S. M. Kuebler, X. Yu, Fabrication of high-aspect-ratio structures using Bessel-beam-activated photopolymerization. *Applied optics* **58** (13), D91–D97 (2019).
36. H. Liu, *et al.*, Filamented light (FLight) biofabrication of highly aligned tissue-engineered constructs. *Advanced Materials* **34** (45), 2204301 (2022).

37. J. F. Heanue, M. C. Bashaw, L. Hesselink, Volume holographic storage and retrieval of digital data. *Science* **265** (5173), 749–752 (1994).
38. L. Shi, B. Li, C. Kim, P. Kellnhofer, W. Matusik, Towards real-time photorealistic 3D holography with deep neural networks. *Nature* **591** (7849), 234–239 (2021).
39. M. Gopakumar, *et al.*, Full-colour 3D holographic augmented-reality displays with metasurface waveguides. *Nature* **629** (8013), 791–797 (2024).
40. A. Majumder, J. A. Doughty, T. M. Hayward, H. I. Smith, R. Menon, Fresnel zone plate outperforms the metalens at high NA. *Optics Express* **33** (11), 23313–23321 (2025).
41. A. Majumder, *et al.*, Color astrophotography with a 100 mm-diameter f/2 polymer flat lens. *Applied Physics Letters* **126** (5) (2025).
42. A. N. Jena, *et al.*, Extended depth-of-focus femtosecond laser pulses for flexible micromachining. *Optics Letters* **50** (15), 4670–4673 (2025).
43. P. Somers, S. Koch, P. Kiefer, M. L. Meretska, M. Wegener, Holographic multi-photon 3D laser nanoprinting—at the speed of light: opinion. *Optical Materials Express* **14** (10), 2370–2376 (2024).
44. D. Zhao, *et al.*, Phase-probability shaping for speckle-free holographic lithography. *Nature Communications* **16** (1), 9318 (2025).
45. R. Rizzo, D. Ruetsche, H. Liu, M. Zenobi-Wong, Optimized photoclick (bio) resins for fast volumetric bioprinting. *Advanced Materials* **33** (49), 2102900 (2021).

## Acknowledgments

The authors acknowledge support from Joseph Jacob and Brian Baker for fabrication of the phase masks.

**Funding:** All authors were funded by NSF Future Manufacturing grant #2229036.

### Author contributions:

DL: Inverse design; Mask fabrication; Resin formulation and characterization; 3D printing system setup; 3D printing experiments; Acquisition, analysis, or interpretation of data; Revising and editing the manuscript critically for intellectual content.

XC: Resin formulation and characterization; 3D printing system setup; 3D printing experiments; Acquisition, analysis, or interpretation of data; Revising and editing the manuscript critically for intellectual content.

COD: Resin formulation and characterization; 3D printing system setup; 3D printing experiments; Acquisition, analysis, or interpretation of data; Revising and editing the manuscript critically for intellectual content.

J-WK: Resin characterization.

KSM: Print characterization.

ZAP: Conception or design of the study; Supervision; Funding acquisition; Revising and editing the manuscript critically for intellectual content.

KSL: 3D printing system setup; 3D printing experiments.

AM: Mask characterization; Acquisition, analysis, or interpretation of data.

CHC: Conception or design of the study; Supervision; Funding acquisition.

MC: Conception or design of the study; Supervision; Funding acquisition; Revising and editing the manuscript critically for intellectual content.

RM: Conception or design of the study; Supervision; Funding acquisition; Revising and editing the manuscript critically for intellectual content.

**Competing interests:** There are no competing interests to declare.

**Data and materials availability:** All data needed to evaluate the conclusions in the paper are present in the paper and/or the Supplementary Materials.

## Materials and Methods

**Fabrication of phase masks:** Phase masks were fabricated via grayscale optical lithography. A 2-inch soda-lime glass substrate was spin-coated with a positive-tone photoresist (MICROPOSIT S1813 G2) at 2000 rpm for 60 s, followed by a soft bake at 110 °C for 2 minutes. Precise control of the resulting topography requires prior calibration of the exposure dose–height relationship, enabling accurate translation of grayscale patterns into continuous surface relief structures. Grayscale optical lithography was performed using a direct-write laser lithography system (DWL 66+, Heidelberg Instruments), which modulates the local exposure dose according to the inverse-designed phase profile. Following exposure, the substrate was post-baked at 50 °C for 1 minute and developed in a 1:1 dilution of AZ developer for 1 minute, yielding the final surface-relief structure.

**Resin preparation:** All reagents were of analytical grade and used as received unless otherwise specified. Phenylbis(2,4,6-trimethylbenzoyl)phosphine oxide (BAPO, 99%, AmBeed) was recrystallized prior to use. 2-Phenoxyethyl acrylate (PEA) was provided by Osaka Organic Chemical Industry Ltd., and dipentaerythritol penta-/hexa-acrylate ( $\leq$ 650 ppm MEHQ inhibitor, Sigma Aldrich) served as the crosslinker. The resin formulation consisted of dipentaerythritol penta-/hexa-acrylate (90 wt%), PEA (10 wt%), and BAPO, mixed in a glass vial on a heat shaker at 50 °C for 1 h. To ensure homogeneity and remove bubbles, the mixture was centrifuged in a speed mixer at 1600 rpm for 10 min. The BAPO concentration was adjusted according to the grayscale holographic pattern, compensating for optical attenuation using the Beer–Lambert law.